Eletrônica de Potência
Open Journal of Power Electronics

Received November 29, 2024; accepted March 13, 2025; Date of publication March 25, 2025.
The review of this paper was arranged by Associate Editor Edivan L. C. da Silva and Editor-in-Chief Heverton A. Pereira.
Digital Object Identifier http://doi.org/10.18618/REP.e202529

Droop-based Control Strategy to operate a DC Nanogrid under the Net Zero Energy Concept

José C. U. Pena [1,*], Jéssica A. A. Silva [1], Mateus P. Dias [1], Debora P. Damasceno [1], Luiza H. S. Santos [1], José A. Pomilio [1]

[1]Universidade Estadual de Campinas, Department of Electrical and Computing Engineering, Campinas – São Paulo, Brazil.

e-mail: jcpena@unicamp.br*, j262748@dac.unicamp.br, Mateuspinheirodias@gmail.com, deborapdamasceno@gmail.com, l264535@dac.unicamp.br, antenor@unicamp.br.
*Corresponding author.

ABSTRACT This work presents a droop-based control strategy for a dc nanogrid designed to operate under the Net Zero Energy (NZE) concept, enabling seamless transitions between grid-connected and islanded modes. The nanogrid integrates photovoltaic (PV) generation, a fast electric vehicle charging station (EVSE), and a battery energy storage system (BESS) into a 700 V dc bus interfacing with the ac grid via a bidirectional three-phase AC-DC converter. An isolated DC-DC converter establishes a secondary 48 V dc bus for powering dc loads. An energy management system (EMS) defines an optimal day-ahead power dispatch for the BESS to meet NZE objectives. At the primary control level, a modified power-to-voltage droop strategy ensures accurate power tracking and parallel operation with the AC-DC converter. This approach enables continuous voltage regulation of the main bus under instantaneous power imbalances caused by schedule deviations or operational mode transitions. Additionally, the proposed strategy eliminates the need for secondary control or high-bandwidth communication. The system is validated through hardware-in-the-loop (HIL) simulations using the Typhoon HIL 604 platform, with the control strategy implemented on a DSP. Real-time simulation results confirm stable performance under various operating conditions, including transitions between modes.

KEYWORDS DC microgrids, power control, droop control, EMS, hardware-in-the-loop, Net-Zero-Energy.

I. INTRODUCTION

Nanogrids are emerging as appealing solutions for small-scale dc systems. Similar to microgrids, nanogrids are power distribution systems capable of operating in both grid-connected (GC) and islanded (IS) modes while integrating distributed energy resources (DERs) and local loads. The particularity of nanogrids lies in their small-scale nature, typically confined to a single house or small building [1], [2], and their operation within a single power domain [3], [4]. DC nanogrids are more common than ac ones due to their higher efficiency in integrating dc-based DERs, such as photovoltaic (PV) systems, fuel cells, and battery energy storage systems (BESS) [5], [6]. However, challenges specific to dc systems remain, including the lack of standardization in voltage levels, protection strategies, power quality and grounding schemes [7]–[10].

A critical aspect of a microgrid is the energy management system (EMS), which defines DERs operations to achieve a specific goal, such as the optimal economical operation [11]–[13]. For nanogrids, the optimization objectives are related to the Net Zero Energy (NZE) concept [4], [12], [14], which focuses on designing and controlling the microgrid to achieve an annual energy consumption equal to or less than on-site renewable energy generation. Therefore, related approaches, such as "Nearly Zero-Energy Building" and "Zero-Emission Building," have also been introduced to align energy performance requirements with long-term climate neutrality goals [15].

A straightforward approach for achieving microgrid optimization goals, including NZE, involves power dispatch, also referred to as day-ahead scheduling, in which an optimization algorithm uses prior information, such as demand profiles, energy prices, and PV forecasting, to generate a power schedule for dispatchable resources [14], [16], [17]. This approach has proven effective in achieving optimization objectives at a low cost, making it appealing for nanogrids [2]. However, since no real-time data are considered when defining the dispatch, actual power values deviate from the forecasted ones, resulting in temporary power imbalances, which can lead to voltage fluctuations [2]. While these instantaneous power imbalances are typically handled by the grid-forming unit, this issue has not been extensively studied in the literature [2]. Nevertheless, due to the limited power ratings of grid-forming units in nanogrids, this subject must be addressed, particularly for critical scenarios where the instantaneous power imbalance exceeds the power rating of the grid-forming units, as when fast-charging EVSE operates [18].

The consideration of real-time data in the EMS, as presented in [19], [20], can resolve these situations; however, this requires fast-response controllable sources and high-bandwidth communication, resulting in a more complex and expensive control system [18]. Such a system may be unsuitable for small-scale microgrids. In [2], a power-balancing optimization process is proposed to compensate for forecasted demand errors in a nanogrid without requiring real-time data. This is achieved by integrating a supercapacitor as a fast-response energy storage system which is also incorporated into the EMS dispatch under a power modulation approach. However, from a practical perspective, the inclusion of a supercapacitor requires an additional power converter and communication lines, thereby increasing the overall cost.

An alternative is to adopt a hierarchical control approach, where the EMS dispatch acts as the tertiary control layer, providing power references for specific dispatchable converters (e.g., BESS, AC/DC), while the inner control layers (secondary and primary) are responsible for ensuring microgrid stability [21]. For the proper implementation of day-ahead dispatch in DC microgrids, the inner control layers must ensure accurate power reference tracking and voltage regulation, even in the presence of critical power imbalances.

Droop control is the most common strategy for the primary control layer in dc microgrids [21], [22]. It is typically used for power sharing and voltage regulation due to its simplicity, enabling the parallel operation of voltage sources. However, the performance of traditional droop strategies is heavily affected by line impedances and voltage deviations, and it is not suitable for tracking power references [22], [23]. These limitations are usually addressed by the secondary control layer [24].

The concept of adaptive droop [6], [25], [26] involves a centralized secondary controller that adjusts the droop gain of the battery converters through low-bandwidth communication. Similarly, studies [27], [28] propose the use of centralized secondary controllers that measure global variables to adjust the references for primary controllers. However, centralized secondary controllers may be affected by communication delays or single points of failure [23], [24]. To address these issues, a distributed secondary control approach has been proposed, as presented in [24], [29], introducing the concepts of virtual-voltage-droop and virtual-current-derivative to improve current sharing. Nevertheless, these droop-based secondary control strategies are not designed for reference tracking, as required for scheduled NZE dispatch.

An example of a droop-free secondary controller applied to DC nanogrids is the distributed price-based power management presented in [4]. In this approach, the power response of the converters is defined by a price matrix, which establishes operational modes. Additionally, the method does not require high-bandwidth communication, as it adopts DC bus signaling (DBS) to update the operation mode [23]. However, it is not intended to work with schedule dispatch EMS, and it does not address the issue related to the forecasted demand error.

On the other hand, for dc nanogrids it is interesting to reduce the complexity of hierarchical control by dismissing the utilization of a dedicated secondary control layer. In this case, the adopted primary control layer should ensure the system stability in both operation modes and during transitions.

In this context, this work proposes a power-droop-based strategy for a dc nanogrid with a single BESS, aiming to achieve NZE operation via a day-ahead dispatch. The proposed approach is based on the parallel operation of converters responsible for dc bus regulation, ensuring continuous voltage control of the main microgrid. Moreover, the proposed strategy is especially intended for dc nanogrids, dismissing a dedicated secondary control layer and high-bandwidth communication. This work builds upon and extends the research presented in [30]. The key improvements include a comprehensive analysis of the impact of adopting EMS methods based on day-ahead dispatch in nanogrids, particularly addressing critical scenarios where these methods may challenge the nanogrid stability. To mitigate these challenges, the paper introduces a straightforward power-to-voltage droop strategy for the BESS. This strategy ensures the achievement of EMS objectives while maintaining system stability, even during unplanned transitions.

II. SYSTEM DESCRIPTION

The general schematics of the studied dc nanogrid are presented in Fig. 1, where the power converters are identified along with the corresponding power variables, and the bidirectional power flow is highlighted with red arrows. This diagram corresponds to the initial conception of a microgrid called DC Nanogrid within the project Microgrids for Efficient, Reliable and Greener Energy (MERGE), intended to demonstrate dc microgrids technologies and management strategies [31].

The DC Nanogrid has a main dc bus of 700 V to integrate all the DERs and an LVDC bus of 48 V. The adoption

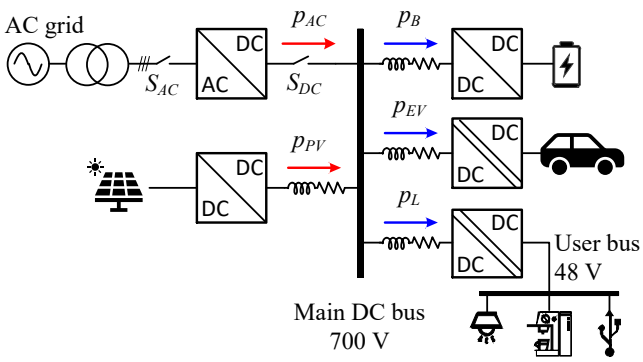

FIGURE 1. General schematics of studied DC Nanogrid

of a 700 V dc bus was primarily driven by the need for compatibility with a three-phase ac 380 V grid and to comply with the recommendations of IEC Technical Report 63282:2024 [10]. The ac-dc converter acts as an interface with the ac utility and is responsible for forming the main dc bus. A bulky line-frequency transformer provides galvanic isolation between the ac utility and the DC Nanogrid.

The DERs integrate into the main dc bus utilizing three power converters: the BESS converter, an isolated converter for EVSE, and a PV converter. An isolated unidirectional step-down converter forms the secondary 48 V-bus to feed user loads such as air conditioning, electronic appliances, and LED lighting [32]. If needed, higher-power loads requiring a voltage supply above 48 V can be directly connected to the main dc bus or through additional dedicated converters. The disconnection devices are S_{AC} for the main ac grid and S_{DC} for the dc bus. The status of S_{DC} defines the microgrid operation mode, IS for open and GC for closed. Table 1 summarizes the main converters that compose the dc microgrid.

The DC Nanogrid is intended to operate under the NZE concept; thus, the PV generation and BESS are designed with the goal that the total energy requirement within a year is supplied locally. Moreover, the BESS is sized to provide the total power and energy demand from the EVSE in both operation modes.

For simplicity, the adopted approach for NZE operation is based on an optimal day-ahead dispatch, defined based on PV and load forecast, to minimize the energy consumption from the grid. The scheduled dispatch defines the power set-points for the BESS converter; thus, from an EMS point of view, only the ac-dc and BESS converters are dispatchable.

The impact of instantaneous power deviations on dc voltage is described in (1), where v^{DC} is the instantaneous dc bus voltage and C_{eq} is the equivalent dc bus capacitance.

$$p^{\mathrm{AC}} + p^{\mathrm{PV}} = p^{\mathrm{B}} + p^{\mathrm{EV}} + p^{\mathrm{L}} + C_{eq}\frac{d(v^{\mathrm{DC}})^2}{dt} \tag{1}$$

The two dispatchable converters are analyzed in detail in the following subsections. In contrast, the others are considered constant power loads (EVSE and dc loads) and sources (PV). The main parameters of the ac-dc converter, designed according to traditional guidelines [33], and the BESS converter are listed in Table 2.

TABLE 1. Converters of the DC Nanogrid

Stage	Topology	Power	Voltage
Main dc bus	unipolar	NA	700 V ±35 V
AC-DC converter	3-ϕ VSI + LCL filter	22 kW	380V @ 60Hz
PV converter	Boost	21.2 kW	330 V
DC Loads	Full Bridge	5 kW	48 V
EVSE	Dual Active Bridge	50 kW	200 to 400 V
BESS	Bidirectional dc-dc	70 kW	400 V

TABLE 2. Main parameters of the dispatchable converters

Converter	Parameter	Value
AC-DC	VSI side inductance (L_1)	400 μH
	Grid side inductance (L_2)	80 μH
	AC filter capacitance (C_2)	15 μF
	AC filter damping (R_d)	0.73 Ω
BESS	Battery voltage (V^{b})	400 V
	Battery side inductance (L_B)	400 μH
	Bus side capacitance (C_B)	4 mF
	Filter inductance (L_{fB})	50 μH
	Filter damping (L_{dB}-r_{dB})	10 μH, 2 Ω
Both	Switching frequency (f_s)	20 kHz

A. AC-DC converter

This converter is the interface with the electrical distribution grid and is intended to operate as the dc grid former when the system is connected to the grid. Due to its control simplicity, the adopted topology is the well-known Voltage Source Inverter (VSI) with a passive damped LCL filter, as depicted in Fig. 2 [34]. The ac power, expressed in the dq frame, is defined in (2). For simplicity, the consumed ac power is approximated to the dc power.

$$p^{\mathrm{AC}} = \frac{3}{2}(v_d^{\mathrm{G}} i_d^{\mathrm{AC}} + v_q^{\mathrm{G}} i_q^{\mathrm{AC}}) \approx p^{\mathrm{DC}} = v^{\mathrm{DC}} i^{\mathrm{DC}} \tag{2}$$

As the power demand for EV charging is supplied by the BESS, the ac-dc converter is rated considering the peak power exportation from local PV generation, which is 22 kW.

B. BESS

The BESS is the component that allows the DC Nanogrid to operate in IS and to achieve the NZE goals. It is designed to supply all the required power by the loads, ensuring at least one daily EV recharge (around 52 kWh); thus, the BESS is sized as 70 kW, 75 kWh.

For simplicity, a non isolated bidirectional dc-dc configuration is adopted as a Power Conversion System (PCS), as depicted in Fig. 3. The corresponding power injected into the main dc bus is defined by (3).

$$p^{\mathrm{B}} = v^{\mathrm{B}} i^{\mathrm{B}} \tag{3}$$

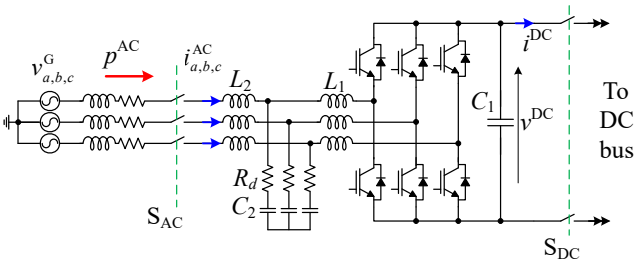

FIGURE 2. Schematics of ac-dc converter.

III. EMS FOR NZE

The EMS in the DC Nanogrid is tasked with optimizing the day-ahead dispatch of DERs to achieve NZE consumption throughout the day (24-hour horizon). This involves effectively coordinating BESS and EV converters' charging and discharging cycles, managing PV generation, and adjusting loads, particularly during islanded conditions.

While short horizons, such as 24 hours, may result in dispatch strategies that exclude grid exchanges and rely solely on local resources, longer horizons, such as a year, necessitate incorporating the accumulated energy balance up to day n when planning for the day $n+1$. This adjustment ensures that the overall energy balance achieves NZE by the end of the defined period.

A. Mathematical Formulation Model

The EMS problem can be modeled as a mixed-integer linear programming (MILP) model, given by (4)-(23). Appendix A describes all the sets, indexes, parameters, and variables. The objective function (4) minimizes total grid energy consumption and power injection into the power grid.

$$\min\left\{\Delta_t\,\Gamma_c \sum_{t\in T}\sum_{o\in O} P^{\text{AC+}}_{t,o} + P^{\text{AC-}}_{t,o}\right\} \tag{4}$$

Constraint (5) represents the power balance in the system, considering the power consumption and injection into the grid, the power from PV generation, the charge or discharge power of the BESS, the charging power of the EV, and loads.

Constraint (6) limits the capacity to inject or withdraw power from the main grid, and constraint (7) divides the active power $P^{\text{AC}}_{t,o}$ into two positive variables, where ($P^{\text{AC+}}_{t,o}$) represents the power demanded from the grid and ($P^{\text{AC-}}_{t,o}$) represents the power injected into the grid, originating from the BESS or PV generation.

$$P^{\text{AC}}_{t,o} + P^{\text{PV}}_{t}\left(1 - x^{\text{PV}}_{t,o}\right) + P^{\text{B-}}_{t} - P^{\text{B+}}_{t} - P^{\text{EV}}_{t,o} = P^{\text{L}}_{t}\left(1 - x^{\text{L}}_{t,o}\right) \quad \forall\, t,o \tag{5}$$

$$P^{\text{AC}}_{t,o} \le \overline{P}^{\text{AC}} \quad \forall\, t,o \tag{6}$$

$$P^{\text{AC}}_{t,o} = P^{\text{AC+}}_{t,o} - P^{\text{AC-}}_{t,o} \quad \forall\, t,o \tag{7}$$

Unexpected disruptions in the main power grid can occur at any moment within the microgrid's operational timeframe. To address this, a set of contingencies (C) is defined, covering all potential periods when a disruption could happen, $C = \{1, ..., T\}$.

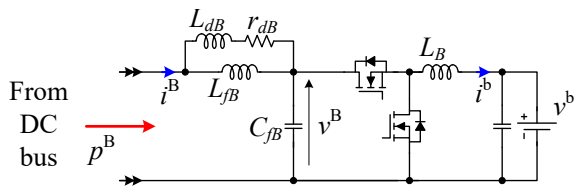

FIGURE 3. Schematics of BESS converter.

The security constraint in (8) ensures that the DC Nanogrid disconnects from the main grid during such events. Additionally, constraint (9) guarantees that there will not be PV generation curtailment during grid-connected operation.

$$P^{\text{AC}}_{t,o} = 0 \quad \forall\, t,o|_{t\ge o \text{ and } t<o+\Delta t_o} \tag{8}$$

$$x^{\text{PV}}_{t,o} = 0 \quad \forall\, t,o|_{t<o \text{ or } t\ge o+\Delta t_o} \tag{9}$$

The constraints (10)–(15) describe the behavior and operation of the BESS. The BESS operates independently of the set of contingencies, as it must be capable of operating optimally under any circumstances. Therefore, external disruptions do not influence its behavior, ensuring reliable performance regardless of the conditions.

Constraints (10) and (11) govern the BESS's state of charge (SoC), with (10) depending on its initial energy and (11) relying on the energy level from the previous time step. The total power exchanged by the BESS is managed through constraint (12), which accounts for the respective efficiencies. Additionally, constraints (13)–(15) define the limits for both energy and charging/discharging power, ensuring these values remain within the designated minimum and maximum capacities.

$$E^{\text{B}}_{t} = E^{\text{B,ini}} + P^{\text{B}}_{t}\,\Delta t \quad \forall t|_{t=1} \tag{10}$$

$$E^{\text{B}}_{t} = E^{\text{B}}_{t-1} + P^{\text{B}}_{t}\,\Delta t \quad \forall t|_{t>1} \tag{11}$$

$$P^{\text{B}}_{t} = P^{\text{B+}}_{t}\,\eta^{\text{B}} - P^{\text{B-}}_{t}\,\frac{1}{\eta^{\text{B}}} \quad \forall t \tag{12}$$

$$\underline{E}^{\text{B}} \le E^{\text{B}}_{t} \le \overline{E}^{\text{B}} \quad \forall t \tag{13}$$

$$\underline{P}^{\text{B+}}\,b^{+}_{t} \le P^{\text{B+}}_{t} \le \overline{P}^{\text{B+}}\,b^{+}_{t} \quad \forall t \tag{14}$$

$$\underline{P}^{\text{B-}}\,b^{-}_{t} \le P^{\text{B-}}_{t} \le \overline{P}^{\text{B-}}\,b^{-}_{t} \quad \forall t \tag{15}$$

The constraints (16)–(21) represent the operation of the EV chargers. The SoC of the EVs is defined by (16) and (17). In addition, (18) and (19) establish limits on energy and charging power, ensuring that these values remain within the EVs' minimum and maximum capacities.

Constraint (20) provides that each EV is fully charged when it departs from the charging station. In contrast, constraint (21) prevents any charging activity outside the specified arrival (t_a) and departure (t_d) times.

$$E^{\text{EV}}_{t,o} = E^{\text{EV,ini}} + P^{\text{EV}}_{t,o}\,\eta^{\text{EV}}\,\Delta t \quad \forall\, t,o|_{t=t_a} \tag{16}$$

$$E^{\text{EV}}_{t,o} = E^{\text{EV}}_{t-1,o} + P^{\text{EV}}_{t,o}\eta^{\text{EV}}\Delta t \quad \forall t,o|_{t>ta \text{ and } t\le t_d} \tag{17}$$

$$\underline{E}^{\text{EV}} \le E^{\text{EV}}_{t,o} \le \overline{E}^{\text{EV}} \quad \forall t,o|_{t>t_a \text{ and } t\le t_d} \tag{18}$$

$$0 \le P^{\text{EV}}_{t,o} \le \overline{P}^{\text{EV}} \quad \forall t|_{t>t_a \text{ and } t\le t_d} \tag{19}$$

$$E^{\text{EV}}_{t,o} = \overline{E}^{\text{EV}} \quad \forall t|_{t=t_d} \tag{20}$$

$$P^{\text{EV}}_{t,o} = 0 \quad \forall t,o|_{t<t_a \text{ and } t\ge t_d} \tag{21}$$

Finally, the binary characteristics of the decision variables are shown in (22) and (23).

$$x^{\mathrm{PV}}_{t,o}, x^{\mathrm{L}}_{t,o} \in \{0,1\} \qquad \forall t, o \quad (22)$$

$$b^{+}_{t}, b^{-}_{t} \in \{0,1\} \qquad \forall t \quad (23)$$

B. Optimal Day-ahead Dispatch

The proposed MILP model was applied to define the optimal dispatch of the DERs in the DC Nanogrid. The formulation was implemented in the PuLP Python programming language [35] and solved with the commercial solver Gurobi [36]. The EMS strategy is validated considering grid-connected, islanded, and transition modes, with three cases: I) without contingencies; II) with a contingency at 00 to 10 hours and III) without contingencies and with energy export to the grid.

Figure 4 shows the optimal day-ahead dispatch for three study cases. In Case I (Fig. 4a), the EV's availability at the charging station is from 16 to 17 hours, with the EV's initial SoC at 40% and the BESS's initial SoC at 28%. To minimize energy consumption and power injection into the grid, PV generation and the BESS supply local demands.

The BESS recharges with excess PV generation and discharges to provide a fast charge for the EV. During the remaining periods of the day, the grid and BESS supply the load to reduce the net energy consumption.

The initial parameters in Case II are: the EV's availability at the charging station is from 12:30 to 17:30 hours, the EV's initial SoC is 0.4%, and the BESS was fully charged.

Figure 4b shows the optimal day-ahead dispatch considering a contingency at 00 to 10 hours. In this case, to guarantee the balance of the system, it was necessary to cut the PV generation; the BESS and the PV generation were able to supply all the load and the demand of the EV.

Case III considers a scenario where the BESS starts the day with a high SoC (60%). Fig. 4c illustrates the optimal dispatch defined by the EMS. As can be observed, based on a forecast of PV generation, the EMS decides to supply the demand during the early hours using energy from the grid. Once PV generation exceeds the demand, the surplus energy is injected into the grid for a certain period. From 11 hours onwards, the BESS uses the excess PV generation to complete its recharge and then discharges to supply the EV demand and the load during the night.

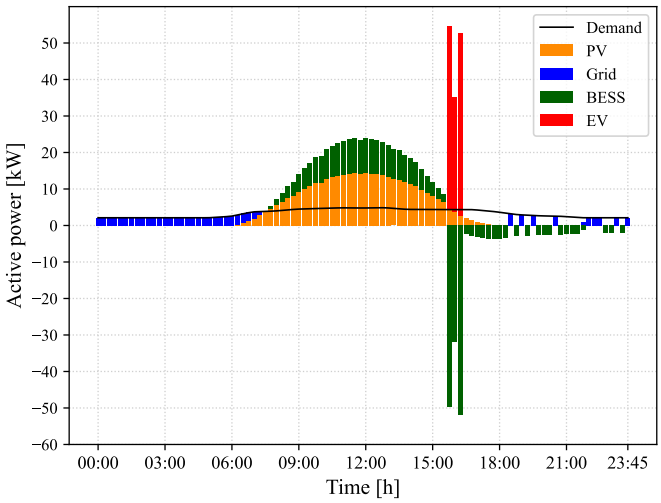

(a) Case I: Operation without contingency

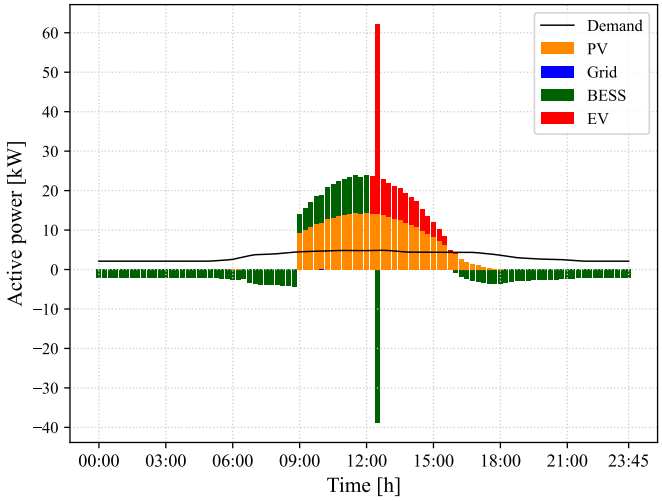

(b) Case II: Operation with contingency at 00:00 to 10:00 hours

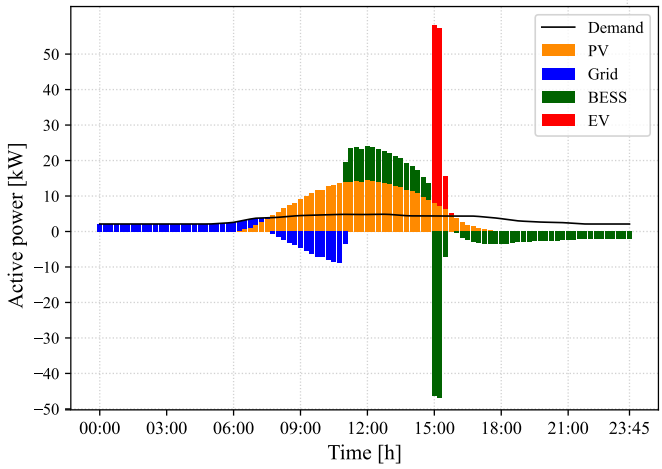

(c) Case III: Operation without contingencies and with energy export

FIGURE 4. Optimal day-ahead dispatch for the grid-connected, islanded, and transition modes.

IV. CONTROL STRATEGY

To effectively manage the control tasks, a power-droop-based control strategy is proposed to enable the parallel operation of the ac-dc and BESS converters.

Each converter regulates its corresponding voltage at the connection point with the dc bus following the reference according to (24), where the uppercase letters are used for references from EMS. In contrast, lower cases are used for primary and inner control loop variables. The parameter K^{x}_{d} is the corresponding power-to-voltage droop gain, and logic variable $E^{\mathrm{x}}_{\mathrm{d}}$ enables the droop control loop. A logic value of 0 disables the droop control; then, the converter operates as a grid former and tightly regulates the corresponding output

voltage. Meanwhile, a logic value of 1 enables the droop control loop.

$$v^{\mathrm{x}}_{ref} = V^{\mathrm{x}} - E^{\mathrm{x}}_{\mathrm{d}} K^{\mathrm{x}}_{d}(P^{\mathrm{x}}_{t} - p^{\mathrm{x}}) \tag{24}$$

With this approach, any instantaneous power imbalances that may produce voltage deviations according to (1) are addressed by the grid-forming converter. For normal operation, only one converter operates as a grid former without droop gain. So, in this approach, droop control is not intended for power sharing.

The droop gains are defined according to (25), where ΔV^{x} is the maximum allowable voltage deviation from nominal voltage and $\overline{P^{\mathrm{x}}}$ is the maximum power.

$$K^{\mathrm{x}}_{d} = \frac{\Delta V^{\mathrm{x}}}{\overline{P^{\mathrm{x}}}} \tag{25}$$

For GC operation, the ac-dc converter operates as the grid former ($E^{\mathrm{AC}}_{\mathrm{d}} = 0$) while the BESS converter operates with droop control. For IS operation, the BESS converter operates as a grid former. The droop control on ac-dc converter is only enabled for planned transitions.

A. Control of the BESS converter

Traditional droop approaches, with proportional gain, fail to zero-error tracking reference in practical dc scenarios. This is due to the inherent resistive behavior of the droop gain with no integrative function in the plant. Thus, a modified power-droop strategy is adopted to regulate the BESS effectively.

A conventional two-loop strategy is adopted for the BESS, as depicted in Fig. 5, with fast inner current control and slower voltage control, typically one decade lower than the current control. Simple proportional plus integral (PI) controllers are adopted for both loops, with transfer functions $G^{\mathrm{B}}_{\mathrm{PI}i}$ and $G^{\mathrm{B}}_{\mathrm{PI}v}$, while the droop transfer function is G^{B}_{d}. The reference signals provided the EMS are highlighted in red.

In GC operation, the output voltage is defined by the ac-dc voltage controller. Thus, the actual voltage value can be considered an external input, as presented in the equivalent control block diagram in Fig. 6, where ideal efficiency has been considered. Moreover, the difference between the output voltage and the BESS external reference can be considered as a disturbance ($\Delta v^{\mathrm{B}} = V^{\mathrm{B}} - v^{\mathrm{B}}$). Then, the corresponding Laplace expression for the supplied power is defined in (26) to (28), where D is the steady-state value of the duty cycle.

$$p^{\mathrm{B}}(s) = P^{\mathrm{B}}_{t}(s) G^{\mathrm{B}}_{p}(s) - \Delta v^{\mathrm{B}} G^{\mathrm{B}}_{pv}(s) \tag{26}$$

$$G^{\mathrm{B}}_{p}(s) = \frac{G^{\mathrm{B}}_{d}(s) G^{\mathrm{B}}_{\mathrm{PI}v}(s) D V^{\mathrm{B}}}{1 + G^{\mathrm{B}}_{d}(s) G^{\mathrm{B}}_{\mathrm{PI}v}(s) D V^{\mathrm{B}}} \tag{27}$$

$$G^{\mathrm{B}}_{pv}(s) = \frac{G^{\mathrm{B}}_{\mathrm{PI}v}(s) D V^{\mathrm{B}}}{1 + G^{\mathrm{B}}_{d}(s) G^{\mathrm{B}}_{\mathrm{PI}v}(s) D V^{\mathrm{B}}} \tag{28}$$

For steady-state conditions and a well-designed PI voltage controller, the power is defined by (29). Under traditional power-droop control, with only proportional gain ($G^{\mathrm{B}}_{d(s\to 0)} = K^{\mathrm{B}}_{d}$), any voltage deviation at the BESS output will have a significant influence in the output power. Typically, this is solved by a secondary controller adjusting the power or voltage reference.

$$p^{\mathrm{B}}_{(s\to 0)} \approx P^{\mathrm{B}}_{t} - \Delta v^{\mathrm{B}} \frac{1}{G^{\mathrm{B}}_{d(s\to 0)}} \tag{29}$$

Aiming to achieve accurate power reference tracking without increasing the control complexity nor requiring a secondary controller, an integral term is included in the droop controller (30). Thus, in steady-state conditions, the transfer function G^{B}_{pv} tends to zero.

The integrator's effect can be considered compensation for the voltage deviation to achieve accurate power tracking within a certain voltage range. The integral gain is defined as equal to the droop gain. However, since the integral component only compensates for the voltage deviation at BESS output, the integrator output is limited to ± 9 V. Thus, the steady-state output power for voltage deviation higher than the integrator range is defined in (31), where v^{B}_{int} is the integrator output limit value.

$$G^{\mathrm{B}}_{d}(s) = K^{\mathrm{B}}_{d} + K^{\mathrm{B}}_{\mathrm{Id}} \frac{1}{s} \tag{30}$$

$$p^{\mathrm{B}}_{(s\to 0)} \approx P^{\mathrm{B}}_{t} - \frac{(V^{\mathrm{B}} - v^{\mathrm{B}} + v^{\mathrm{B}}_{int})}{K^{\mathrm{B}}_{d}} \tag{31}$$

The BESS control parameters are listed in Table 3. The PI gains have been computed for bandwidths of 2 kHz at the current controller and 200 Hz at the voltage controller.

In case the v^{DC} is not tightly regulated, as during planned transitions, it is not possible to track the power reference, and the corresponding tracking error will produce a voltage deviation. To keep this deviation within the operational limits of Table 1, a saturation block is used at the droop controller output with limits ΔV^{B}.

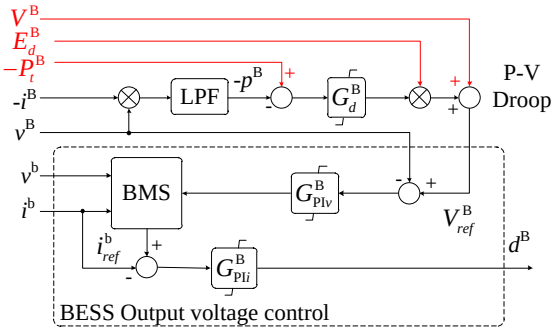

FIGURE 5. Block diagram of the BESS controller.

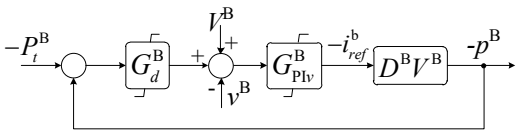

FIGURE 6. Equivalent Block diagram of BESS power control in GC mode.

The preceding analysis has not considered the influence of the propagation delay of the reference signal from the EMS to the primary control. This subject is relevant for coordination between secondary and primary control layers, as presented in [29]. However, while propagation delay contributes to discrepancies between forecasted and actual values, its effect is limited to a millisecond timescale, whereas critical power imbalances occur over much longer timescales. In this context, explicitly including propagation delay does not provide significant analytical advantages for studying the critical scenarios for voltage regulation.

B. Control of the AC-DC converter

To operate this converter as the grid former in GC operation, a traditional two-loop control strategy is adopted, with an inner fast ac current loop in the dq-frame (i_d^{AC} and i_q^{AC}) and a slower dc voltage (v^{DC}) control loop. Simple proportional plus integral (PI) controllers are adopted for both loops. The dc voltage controller is tuned for 20 Hz while the inner current controller is tuned for 2 kHz bandwidth. Feedforward decoupling terms are included in the current controller [33] to achieve a fast response.

The outer power-voltage droop loop is based on measuring the dc power and considers only proportional gain since it is intended only for planned transitions. The controller gains of the ac-dc converter are listed in Table 3. The corresponding block diagram of the ac-dc controller is presented in Fig. 7.

C. Bus voltage control

1) Grid connected operation

In GC mode, the AC-DC converter tightly regulates the bus voltage by compensating for power imbalances. At the same time, the BESS operates with a power-voltage droop to track the day-ahead dispatch reference. However, critical conditions may arise due to forecasted demand errors during EVSE turn-on and turn-off since EV converter's power rating exceeds the AC-DC converter's capacity.

TABLE 3. Controllers parameters

Stage	Parameter	Value
AC-DC	Current proportional gain ($K_{\mathrm{P}i}^{\mathrm{AC}}$)	4.1
	Current integral gain ($K_{\mathrm{I}i}^{\mathrm{AC}}$)	3085
	Voltage proportional gain ($K_{\mathrm{P}v}^{\mathrm{AC}}$)	0.84
	Voltage integral gain ($K_{\mathrm{I}v}^{\mathrm{AC}}$)	10.72
	Droop gain (K_d^{AC})	1.6 mV/W
BESS	Current proportional gain ($K_{\mathrm{P}i}^{\mathrm{B}}$)	8 m
	Current integral gain ($K_{\mathrm{I}i}^{\mathrm{B}}$)	10
	Voltage proportional gain ($K_{\mathrm{P}v}^{\mathrm{B}}$)	8.5
	Voltage integral gain ($K_{\mathrm{P}v}^{\mathrm{B}}$)	1000
	Droop gain (K_d^{B})	0.5 mV/W
	Droop integral gain ($K_{\mathrm{I}d}^{\mathrm{B}}$)	0.5 mV/Ws
	Droop limits (ΔV^{B})	±35 V

The management of these conditions is outlined below, with the corresponding waveforms illustrated in Fig. 8. For simplicity, it is assumed that the BESS output voltage equals the main dc bus voltage, and losses are dismissed. The dc loads and PV generation remain constant.

Before the EVSE turn-on, the BESS operate with reference P_{n-1}^{B} and p^{AC} is almost zero. At t_{on}^{EV}, the EVSE starts, increasing power demand. Initially, the AC-DC converter addresses the mismatch, but at t_1, it reaches its maximum power ($\overline{P}^{\mathrm{AC}}$). From t_1 to t_2, the EVSE's increasing demand lowers the bus voltage according to (1), causing the BESS droop controller to respond by increasing its power output per (26). At t_2, the EVSE stabilizes at maximum power, reaching a new equilibrium defined by (31) and (32). The bus voltage returns to its nominal value once the BESS reference updates at t_n.

$$V_{\mathrm{on}}^{\mathrm{DC}} = V^{\mathrm{DC}} + K_d^{\mathrm{B}}(P_{\mathrm{EVon}}^{\mathrm{B}} - P_{n-1}^{\mathrm{B}}) - v_{int}^{\mathrm{B}} \tag{32}$$

Similarly, during EVSE turn-off, at t_{off}, power demand from the grid decreases. Between t_{off}^{EV} and t_3, the ac-dc converter manages the imbalance, eventually exporting power to the grid up to reaching the maximum power at t_3. Beyond that, excess power increases the bus voltage per (1), prompting the BESS droop controller to reduce the injected power according to (26). At t_4, a new equilibrium is reached per (33). When the BESS reference updates at t_{n+1}, the bus voltage is restored to nominal.

$$V_{\mathrm{off}}^{\mathrm{DC}} = V^{\mathrm{DC}} + K_d^{\mathrm{B}}(P_{\mathrm{EVoff}}^{\mathrm{B}} - P_n^{\mathrm{B}}) + v_{int}^{\mathrm{B}} \tag{33}$$

2) Islanded operation

In IS operation, the switch $\mathrm{S_{DC}}$ remains open and the BESS converter regulates the dc bus voltage ($E_d^{\mathrm{B}} = 0$). The main challenge arises when PV generation exceeds the allowable power for BESS charging due to high SOC. In this condition, the EMS commands the curtailment of the PV generation. An example of this condition is presented in Fig. 4(b).

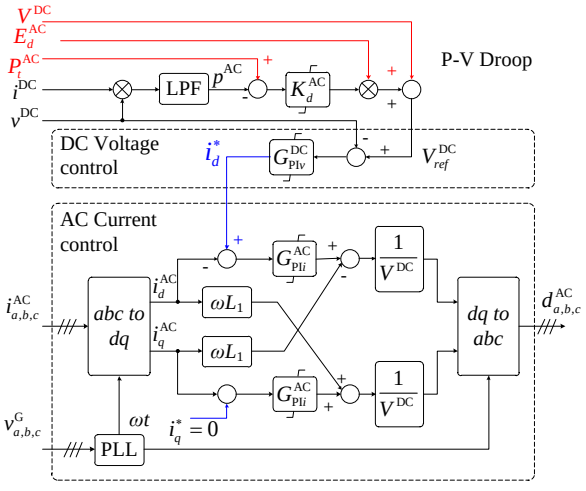

FIGURE 7. Block diagram of the ac-dc controller.

D. Transitions

A major feature of droop-based control strategies is the continuous regulation of the dc bus voltage. This feature allows seamless transitions between operating modes.

1) Unplanned islanding

Following the approach of Fig. 8, the unplanned transition can be considered as the sudden variation of p^{AC} from the current value to zero, which is seen as load step by the BESS converter. This load variation produces a power tracking error and a voltage deviation on v^{B}. Once the EMS has detected the islanding condition, $\mathrm{S_{DC}}$ is opened, and the signal E_d^{B} is disabled to operate the BESS as a grid former.

2) Grid reconnection

During IS operation ($\mathrm{S_{DC}}$ open) the AC-DC converter is turn-on with droop enable ($E_d^{\mathrm{AC}} = 1$) and zero power reference. Then the $\mathrm{S_{DC}}$ is closed. Then, states of enable signals are inverted to operate the BESS converter in droop and the AC-DC converter as the grid former.

V. HIL SIMULATION RESULTS

The DC Nanogrid is modeled and simulated in the HIL platform Typhoon HIL 604 to validate the proposed control strategy. Detailed switched models are considered for all the power converters. For simplicity, isolated power converters (48 Vdc Loads and EVSE) are represented for equivalent buck converters. The local PV generation is represented by a detailed model, considering the dynamic behavior of the PV modules and the realization of the Maximum Power Point Tracking (MPPT) routine. The switching and sampling frequency were set at 20 kHz. With this configuration the model occupies five Standard Processing Cores (SPCs) from a total of eight. The achieved simulation step was 0.5 μs, the lowest possible with the selected HIL platform.

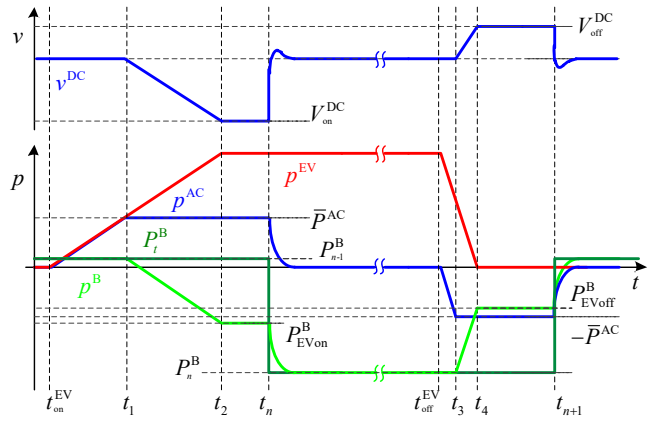

FIGURE 8. Expected voltage and power waveforms for EV turn-on and turn-off.

The proposed control strategy for the ac-dc converter and BESS are implemented in a DSP Texas TMS320F28335. The control strategies of the other converters are implemented in the HIL model. The results presented in this section correspond GC operation, unplanned islanding transition and grid re-connection.

A. Voltage and power control

The power control strategy is validated for power and voltage regulation in GC mode during the two critical conditions: EV turn-on and EV turn-off. The test conditions correspond to the dispatch of Fig. 4(a). The EVSE is turned on around the 63^{th} time interval while it is turned off around the 66^{th}. The scheduled and predicted values for these scenarios are listed in Table 4. The main waveforms are the BESS converter output voltage and power (green), the dc bus voltage and power at ac-dc converter (blue), and the power supplied to the EV converter (red). For simplicity, it is assumed that the BESS power reference is updated a few seconds after the equilibrium point is achieved.

1) EV turn-on

Figure 9 presents the main results for the EV turn-on scenario. Initially, the ac power is near zero, with PV generation around 6.4 kW supplying the dc loads (4.36 kW) and charging the BESS (2 kW). Due to the low output power, the BESS voltage is close to the main dc voltage ($v^{\mathrm{B}} \approx v^{\mathrm{DC}}$).

In $t = 2$ s the EVSE is turned on, causing a gradual increase in power demand while the voltage remains nearly constant. Around $t = 7.5$ s, the ac-dc converter reaches its power limit, decreasing bus voltage. At this point, the BESS supplies the additional power the EVSE requires. This condition persists until the EV power reaches its rated value at approximately $t = 15$ s. The voltage slope changes around $t = 11$ s when the voltage deviation at the BESS output reaches approximately -9 V, highlighting the constrained action of the integrator within the droop power controller. After $t = 15$ s, a new equilibrium point is established, defined by (32) and (34). The maximum voltage deviation in the main bus is -30 V, within the limits of Table 1.

$$p_x^{\mathrm{B}} \approx 2\ \mathrm{kW} - \frac{(700\ \mathrm{V} - 674\ \mathrm{V} - 9\ \mathrm{V})}{0.5\ \mathrm{mV/W}} = -32\ \mathrm{kW} \quad (34)$$

The BESS power reference is updated in $t = 19$ s, restoring the nominal voltage at the main dc bus. As the BESS supplies 50 kW, voltage deviation is evident at the

TABLE 4. Scheduled and predicted values around EV turn-on and turn-off

Interval:	63	64	66	67
P_t^{B} (kW)	2.03	-49.71	-51.79	-2.39
P_t^{EV} (kW)	0	50	50	0
P_t^{PV} (kW)	6.4	4.65	2.56	1.96
P_t^{DC} (kW)	4.36	4.36	4.35	4.34

corresponding output. The results confirm the prediction presented in Fig. 8.

2) EV turn-off

For the turn-off procedure, the main waveforms are presented in Fig. 10. The results are similar; after $t = 2$ s, EVSE power begins to decrease until it reaches zero, while the excess power from the BESS is injected into the ac grid. Around $t = 6$ s, p^{AC} reaches its limit, causing the dc voltage to rise and producing a deviation that the BESS controller attempts to compensate by reducing the supplied power.

This condition persists until approximately $t = 9$ s, when p^{AC} reaches zero. Following (33), the new equilibrium point corresponds to a 24 kW supplied by the BESS (35) and a maximum deviation of 18 V at the main bus. As predicted, when the BESS power reference is updated (around $t = 14$ s), bus voltage returns to its nominal value.

$$p_x^{\mathrm{B}} \approx -50\ \mathrm{kW} - \frac{(700\ \mathrm{V} - 722\ \mathrm{V} + 9\ \mathrm{V})}{0.5\ \mathrm{mV/W}} = -24\ \mathrm{kW} \quad (35)$$

B. Transitions

1) Unplanned islanding

To evaluate the control response during unplanned islanding under critical conditions, the initial scenario considers peak PV generation (21.8 kW), a local load of 4.3 kW, BESS recharging with 1.5 kW and 16 kW exported to ac grid.

The main results for the islanding event are presented in Fig. 11. Upon the disconnection of S_{DC}, the BESS converter enters into grid-former mode by disabling the droop controller. A transient voltage deviation reaches a peak of 8.02 V, around 1.15 %. PV generation remains constant at 21.2 kW and is fully absorbed by the BESS within 10 ms.

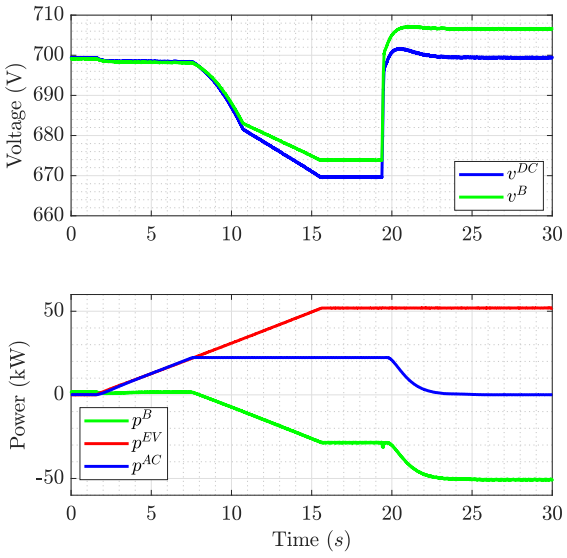

FIGURE 9. Main waveforms for voltage and power control during EVSE turn-on.

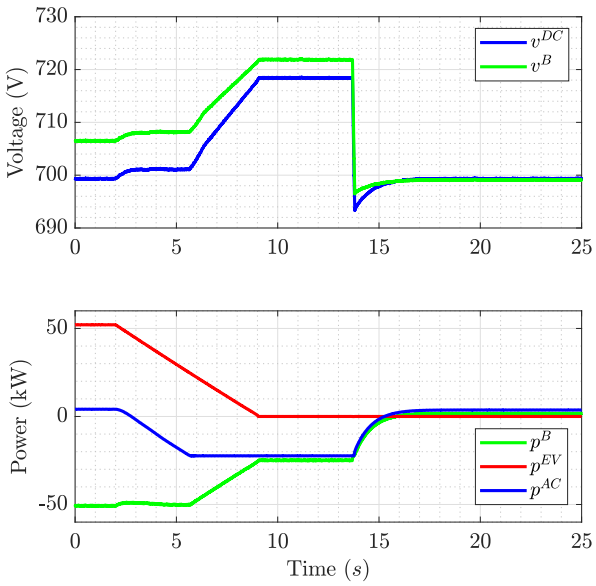

FIGURE 10. Main waveforms for voltage and power control during EVSE turn-off.

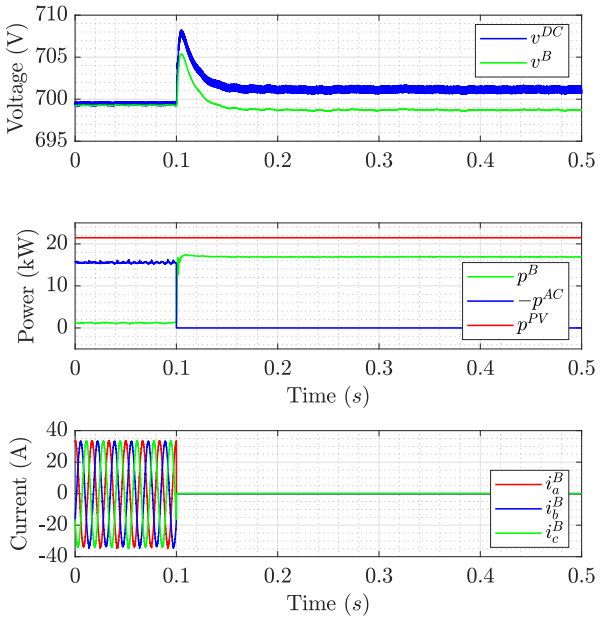

FIGURE 11. Main waveforms for Islanding with peak PV generation.

These results confirm that the proposed control strategy enables a smooth islanding transition, ensuring uninterrupted operation of both local loads and generation.

2) Grid re-connection

The grid reconnection test follows the scenario from the previous section, with the BESS converter operating as a grid-forming unit, a local load of 4.3 kW, and peak PV generation (21.2 kW). The main results are divided into two stages, as shown in Figs. 12 and 13.

In Fig. 12, the grid is assumed to be reestablished, with the ac-dc converter regulating the dc voltage under droop control. At $t = 0.1$ s, the S_{DC} switch closes, transitioning the system to GC mode while the BESS converter remains in grid-forming mode. A minor voltage deviation with a peak value of -2 V occurs, along with a transient power deviation from the BESS peaking at approximately -6 kW before settling at -700 W, now supplied by the ac grid. Throughout the process, PV generation remains constant.

Figure 13 illustrates the second stage of the grid-reconnection process, where control loops for regular GC operation are restored. In $t = 0.1$ s, the BESS droop controller is activated with its corresponding reference P_t^{B}. After 120 ms, the ac-dc converter transitions to grid-forming mode by disabling its droop controller.

During $t = 0.1$ s to $t = 0.23$ s, the converters operate in power-sharing mode, with part of the PV generation exported to the grid. However, as the BESS power cannot be directly controlled, the bus voltage rises to a new equilibrium point, causing a transient power deviation in the BESS with a peak of approximately -13 kW. Once the ac-dc converter takes over as the grid-forming unit, the bus voltage returns to its nominal value, and the BESS power stabilizes according to the reference. These results confirm a smooth and controlled transition from IS to GC mode.

VI. CONCLUSION

This work presents a droop-based control strategy for operating a dc microgrid under the NZE concept, assuming NZE is achieved through an optimal day-ahead dispatch. Using historical and forecast data, the EMS defines a 15-minute dispatch schedule for the BESS to minimize energy consumption and grid export. However, as the dispatch does not consider real-time data, power imbalances are anticipated.

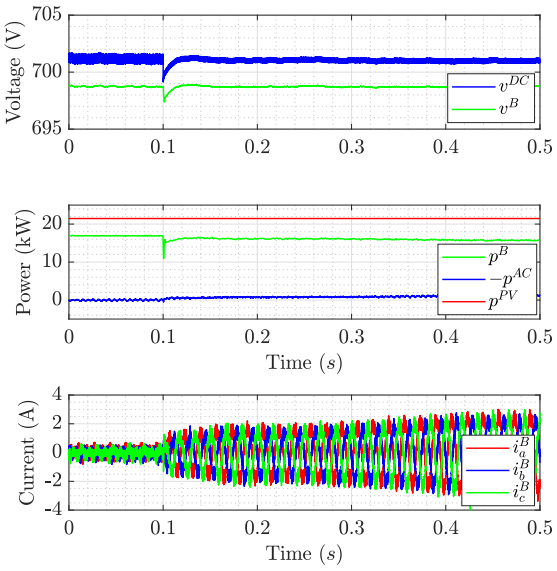

FIGURE 12. Main waveforms for grid re-connection with PV peak generation: Transition.

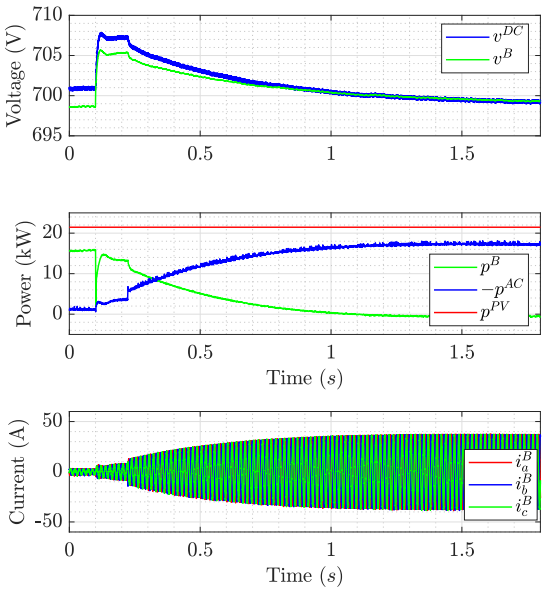

FIGURE 13. Main waveforms for grid re-connection with PV peak generation: Restoring the droop control on the BESS converter.

The proposed control strategy enables parallel operation of the ac-dc and BESS converters. In GC mode, the ac-dc converter acts as the main grid-forming unit without droop control, while the BESS converter uses a modified PI-based power-voltage droop. This ensures accurate BESS power tracking of EMS references and continuous voltage regulation, even during power imbalances caused by forecasted demand errors or critical conditions like EV recharging. The additional constrained integrator in the droop controller compensates voltage deviations, ensuring accurate power regulation while preserving droop control benefits, allowing seamless transitions between operating modes. Furthermore, the proposed control strategy is implemented at the primary control level, requiring no additional high-bandwidth communication apart from the reference from the EMS.

The proposed approach was validated through real-time simulation using the Typhoon HIL 604 Hardware-in-the-Loop platform, which incorporates switched models for all power converters and the connection impedance to the microgrid bus. Additionally, the control strategy was implemented on a DSP.

Simulation results demonstrate that the system performs as expected, ensuring accurate control of BESS power to follow the dispatch schedule and maintain stable operation under critical conditions, such as instantaneous power imbalances caused by schedule mismatches or during transitions.

These results confirm the effectiveness of the proposed control strategy and demonstrate the utility of the HIL microgrid model for analyzing system dynamics under various management strategies, serving as a critical step before practical deployment. As a continuation of this research, a reduced-scale experimental setup is being developed to validate the strategy and compare its performance with

alternative approaches, particularly those using secondary controllers to mitigate voltage deviations.

APPENDIX A - Nomenclature

Sets and Indexes

O, o	Set of outages, $o \in O$
T, t	Set of time intervals, $t \in T$

Parameters

Δ_t	Duration of each time step [min]
Δt_o	Duration of each time contingency [min]
η^{B}	Efficiency of the BESS [%]
η^{EV}	Efficiency of the EV [%]
$\overline{E}^{\mathrm{B}}$	Maximum energy capacity of the BESS [kWh]
$\overline{E}^{\mathrm{EV}}$	Maximum energy capacity of the EV [kWh]
$\overline{P}^{\mathrm{B}\text{-}}$, $\overline{P}^{\mathrm{B}+}$	Maximum dis/charging power of the BESS [kW]
$\overline{P}^{\mathrm{EV}}$	Maximum charging power of the EV charger [kW]
$\overline{P}^{S}$	Maximum capacity of the main grid [kW]
$\underline{E}^{\mathrm{B}}$	Minimum energy capacity of the BESS [kWh]
$\underline{E}^{\mathrm{EV}}$	Minimum energy capacity of the EV [kWh]
$\underline{P}^{\mathrm{B}\text{-}}$, $\underline{P}^{\mathrm{B}+}$	Minimum dis/charging power of the BESS [kW]
Γ_c	Probability of each contingency [-]
$E^{\mathrm{B,ini}}$	Initial energy of the BESS [kWh]
$E_s^{\mathrm{EV,ini}}$	Initial energy of the EV [kWh]
P_t^{L}	Active power demand [kW]
P_t^{PV}	Active PV generation [kW]
t_a	EV time arrival of the charger station [h]
t_d	EV time departure of the charger station [h]

Variables

b_t^+, b_t^-	BESS charging and discharging operation [-]
E_t^{B}	Energy of the BESS [kWh]
$E_{t,o}^{\mathrm{EV}}$	Energy of the EV [kWh]
$P_{t,o}^{\mathrm{AC}}$	Active power at the grid [kW]
$P_t^{\mathrm{B}\text{-}}$, $P_t^{\mathrm{B}+}$	BESS discharging and charging power[kW]
$P_{t,o}^{\mathrm{EV}}$	Charging power of the EV charger [kW]
$x_{t,o}^{\mathrm{PV}}$	Decision binary variable for PV generation reduction [-]
$x_{s,t,o}^{L}$	Decision binary variable for load curtailment [-]

ACKNOWLEDGMENT

This work was developed under the Electricity Sector Research and Development Program PD-00063-3058/2019 - PA3058: "MERGE - Microgrids for Efficient, Reliable and Greener Energy" ANEEL, in partnership with CPFL Energia. This work has also been supported by FAPESP (grants: 2022/03441-7, 2023/13444-6; thematic project: 2021/11380-5).

AUTHOR'S CONTRIBUTIONS

J.C.U.PENA: Conceptualization, Formal Analysis, Investigation, Methodology, Validation, Writing – Original Draft, Writing – Review & Editing. **J.A.A.SILVA:** Formal Analysis, Investigation, Methodology, Software, Writing – Original Draft, Writing – Review & Editing. **M.P.DIAS:** Methodology, Visualization, Writing – Original Draft, Writing – Review & Editing. **D.P.DAMASCENO:** Methodology, Visualization, Writing – Original Draft, Writing – Review & Editing. **L.H.S.SANTOS:** Methodology, Visualization, Writing – Original Draft, Writing – Review & Editing. **J.A.POMILIO:** Investigation, Methodology, Supervision, Visualization, Writing – Original Draft, Writing – Review & Editing.

PLAGIARISM POLICY

This article was submitted to the similarity system provided by Crossref and powered by iThenticate – Similarity Check.

REFERENCES

[1] D. Burmester, R. Rayudu, W. Seah, D. Akinyele, "A review of nanogrid topologies and technologies", *Renewable and Sustainable Energy Reviews*, vol. 67, pp. 760–775, 2017, doi:10.1016/j.rser.2016.09.073.

[2] J. Yim, S. You, F. Blaabjerg, Y. Lee, Y. Gui, W. Kim, "Energy management systems for forecasted demand error compensation using hybrid energy storage system in nanogrid", *Renewable Energy*, vol. 221, no. C, 2024, doi:10.1016/j.renene.2023.119, URL: https://ideas.repec.org/a/eee/renene/v221y2024ics0960148123016592.html.

[3] Y. Dafalla, B. Liu, D. A. Hahn, H. Wu, R. Ahmadi, A. G. Bardas, "Prosumer Nanogrids: A Cybersecurity Assessment", *IEEE Access*, vol. 8, pp. 131150–131164, 2020, doi:10.1109/ACCESS.2020.3009611.

[4] E. L. Carvalho, L. V. Bellinaso, R. Cardoso, L. Michels, "Distributed Price-Based Power Management for Multibuses DC Nanogrids EEMS", *IEEE Journal of Emerging and Selected Topics in Power Electronics*, vol. 10, no. 5, pp. 5509–5521, 2022, doi:10.1109/JESTPE.2022.3152101.

[5] M. Mokhtar, M. I. Marei, A. A. El-Sattar, "An Adaptive Droop Control Scheme for DC Microgrids Integrating Sliding Mode Voltage and Current Controlled Boost Converters", *IEEE Trans Smart Grid*, vol. 10, no. 2, pp. 1685–1693, 2019, doi:10.1109/TSG.2017.2776281.

[6] T. Dragičević, J. M. Guerrero, J. C. Vasquez, D. Škrlec, "Supervisory Control of an Adaptive-Droop Regulated DC Microgrid With Battery Management Capability", *IEEE Trans Power Electron*, vol. 29, no. 2, pp. 695–706, 2014, doi:10.1109/TPEL.2013.2257857.

[7] A. Saxena, N. K. Sharma, S. R. Samantaray, "An Enhanced Differential Protection Scheme for LVDC Microgrid", *IEEE J Emerg and Sel Topics Power Electron*, vol. 10, no. 2, pp. 2114–2125, 2022, doi:10.1109/JESTPE.2022.3144300.

[8] T. Dragičević, X. Lu, J. C. Vasquez, J. M. Guerrero, "DC Microgrids—Part II: A Review of Power Architectures, Applications, and Standardization Issues", *IEEE Trans Power Electron*, vol. 31, no. 5, pp. 3528–3549, 2016, doi:10.1109/TPEL.2015.2464277.

[9] D. P. Damasceno, P. Sbabo, M. P. Dias, J. C. U. Peña, J. F. Guerreiro, P. Mattavelli, J. A. Pomilio, "DC Bus Voltage High-Frequency Disturbances Analysis for DC Microgrids With Long Connections", *IEEE Open Journal of Power Electronics*, vol. 6, pp. 371–382, 2025, doi:10.1109/OJPEL.2025.3540347.

[10] PD-IEC-TR-63282:2024, *LVDC systems — Assessment of standard voltages and power quality requirements*, International Electrotechnical Commission, 8 2024.

[11] H. C. Jo, G. Byeon, J. Y. Kim, S. K. Kim, "Optimal Scheduling for a Zero Net Energy Community Microgrid with Customer-Owned Energy Storage Systems", *IEEE Trans Power Syst*, vol. 36, pp. 2273–2280, 5 2021, doi:10.1109/TPWRS.2020.3036077.

[12] J. Wu, Y. Zhou, W. Gan, "Smart Local Energy Systems Towards Net Zero: Practice and Implications from the UK", *CSEE Journal of Power and Energy Systems*, vol. 9, pp. 411–419, 3 2023, doi:10.17775/CSEEJPES.2022.08420.

[13] J. A. A. Silva, J. C. López, C. P. Guzman, N. B. Arias, M. J. Rider, L. C. da Silva, "An IoT-based energy management system for AC microgrids with grid and security constraints", *Applied Energy*, vol. 337, p. 120904, 5 2023, doi:10.1016/j.apenergy.2023.120904.

[14] L. Li, Y. Han, Q. Li, W. Chen, "Multi-Dimensional Economy-Durability Optimization Method for Integrated Energy and Transportation System of Net-Zero Energy Buildings", *IEEE Transactions on Sustainable Energy*, vol. 15, no. 1, pp. 146–159, 2024, doi:10.1109/TSTE.2023.3275160.

[15] A. Esser, A. Dunne, T. Meeusen, D. W. Simon Quaschning, A. Hermelink, S. Schimschar, M. Offermann, A. John, M. Reiser, A. Pohl, J. Grözinger, *Comprehensive study of building energy renovation activities and the uptake of nearly zero-energy buildings in the EU : final report*, European Commission and Directorate-General for Energy, 2019, doi:10.2833/14675.

[16] E. Nasrolahpour, J. Kazempour, H. Zareipour, W. D. Rosehart, "A Bilevel Model for Participation of a Storage System in Energy and Reserve Markets", *IEEE Transactions on Sustainable Energy*, vol. 9, no. 2, pp. 582–598, 2018, doi:10.1109/TSTE.2017.2749434.

[17] B. Papari, C. S. Edrington, I. Bhattacharya, G. Radman, "Effective Energy Management of Hybrid AC–DC Microgrids With Storage Devices", *IEEE Transactions on Smart Grid*, vol. 10, no. 1, pp. 193–203, 2019, doi:10.1109/TSG.2017.2736789.

[18] K. Mahmud, J. Ravishankar, M. J. Hossain, Z. Y. Dong, "The Impact of Prediction Errors in the Domestic Peak Power Demand Management", *IEEE Transactions on Industrial Informatics*, vol. 16, no. 7, pp. 4567–4579, 2020, doi:10.1109/TII.2019.2946292.

[19] I. Bendato, A. Bonfiglio, M. Brignone, F. Delfino, F. Pampararo, R. Procopio, "A real-time Energy Management System for the integration of economical aspects and system operator requirements: Definition and validation", *Renewable Energy*, vol. 102, pp. 406–416, 2017, doi:10.1016/j.renene.2016.10.061.

[20] C. L. Nge, I. U. Ranaweera, O.-M. Midtgård, L. Norum, "A real-time energy management system for smart grid integrated photovoltaic generation with battery storage", *Renewable Energy*, vol. 130, pp. 774–785, 2019, doi:10.1016/j.renene.2018.06.073.

[21] J. C. Neves, R. D. Silveira, S. A. O. da Silva, L. P. Sampaio, "Estudo e Implementação de Controle Secundário em Microrredes CC", *Eletrônica de Potência*, vol. 29, p. e202416, Jun. 2024, doi:10.18618/REP.2005.1.053061, URL: https://journal.sobraep.org.br/index.php/rep/article/view/921.

[22] L. Xing, Z. Shu, J. Fang, C. Wen, C. Zhang, "Distributed control of DC microgrids: A relaxed upper bound for constant power loads", *Automatica*, vol. 173, p. 112021, 2025, doi:10.1016/j.automatica.2024.112021.

[23] S. K. Sahoo, A. K. Sinha, N. K. Kishore, "Control Techniques in AC, DC, and Hybrid AC–DC Microgrid: A Review", *IEEE Journal of Emerging and Selected Topics in Power Electronics*, vol. 6, no. 2, pp. 738–759, 2018, doi:10.1109/JESTPE.2017.2786588.

[24] L. Xing, J. Cai, X. Liu, J. Fang, Y.-C. Tian, "Distributed Secondary Control of DC Microgrid via the Averaging of Virtual Current Derivatives", *IEEE Transactions on Industrial Electronics*, vol. 71, no. 3, pp. 2914–2923, 2024, doi:10.1109/TIE.2023.3269470.

[25] J. P. Silveira, P. dos Santos Neto, T. Barros, E. Filho, "Power management of energy storage system with modified interlinking converters topology in hybrid AC/DC microgrid", *International Journal of Electrical Power & Energy Systems*, vol. 130, p. 106880, 09 2021, doi:10.1016/j.ijepes.2021.106880.

[26] B. C. Moura, P. J. dos Santos Neto, D. B. Rodrigues, C. Guimarães, L. C. G. Freitas, J. P. C. Silveira, G. B. de Lima, "Evaluating Adaptive Droop Control for Steady-State Power Balancing in DC Microgrids Using Controller Hardware-in-the-Loop", *Eletrônica de Potência*, vol. 29, p. e202451, Dec. 2024, doi:10.18618/REP.e202451, URL: https://journal.sobraep.org.br/index.php/rep/article/view/974.

[27] F. Gao, S. Bozhko, A. Costabeber, C. Patel, P. Wheeler, C. I. Hill, G. Asher, "Comparative Stability Analysis of Droop Control Approaches in Voltage-Source-Converter-Based DC Microgrids", *IEEE Trans Power Electron*, vol. 32, no. 3, pp. 2395–2415, 2017, doi:10.1109/TPEL.2016.2567780.

[28] F. Gao, S. Bozhko, G. Asher, P. Wheeler, C. Patel, "An Improved Voltage Compensation Approach in a Droop-Controlled DC Power System for the More Electric Aircraft", *IEEE Transactions on Power Electronics*, vol. 31, no. 10, pp. 7369–7383, 2016, doi:10.1109/TPEL.2015.2510285.

[29] L. Xing, F. Guo, X. Liu, C. Wen, Y. Mishra, Y.-C. Tian, "Voltage Restoration and Adjustable Current Sharing for DC Microgrid With Time Delay via Distributed Secondary Control", *IEEE Transactions on Sustainable Energy*, vol. 12, no. 2, pp. 1068–1077, 2021, doi:10.1109/TSTE.2020.3032605.

[30] J. C. U. Peña, M. P. Dias, D. P. Damasceno, J. I. Y. Ota, J. A. Pomilio, "Control Strategy and Hardware-in-the-Loop Simulation of a DC Microgrid Under the Net Zero Energy Concept", *in 2023 IEEE 8th Southern Power Electronics Conference and 17th Brazilian Power Electronics Conference (SPEC/COBEP)*, pp. 1–7, 2023, doi:10.1109/SPEC56436.2023.10407571.

[31] J. C. López, J. I. Y. Ota, M. J. Rider, J. A. Pomilio, L. C. P. da Silva, R. G. Bento, "Objetivos e Desafios do Projeto de P&D MERGE: Microgrids for Efficient, Reliable and Greener Energy", *in Anais do Simpósio Brasileiro de Sistemas Elétricos 2020*, SBA, 8 2020, doi:10.48011/sbse.v1i1.2313.

[32] E. L. Carvalho, A. Blinov, A. Chub, P. Emiliani, G. de Carne, D. Vinnikov, "Grid Integration of DC Buildings: Standards, Requirements and Power Converter Topologies", *IEEE Open Journal of Power Electronics*, vol. 3, pp. 798–823, 2022, doi:10.1109/OJPEL.2022.3217741.

[33] M. Liserre, F. Blaabjerg, S. Hansen, "Design and control of an LCL-filter-based three-phase active rectifier", *IEEE Trans Ind Appl*, vol. 41, pp. 1281–1291, 2005, doi:10.1109/TIA.2005.853373.

[34] J. C. U. Peña, L. P. Sampaio, M. A. G. de Brito, C. A. Canesin, "Robust Control of Three-Phase VSI with LCL Filter for Distributed Generation Power Quality Improvement", *Journal of Control, Automation and Electrical Systems*, vol. 31, pp. 1051–1062, 8 2020, doi:10.1007/s40313-020-00610-y.

[35] S. Mitchell, A. Kean, A. Mason, M. O'Sullivan, A. Phillips, F. Peschiera, "Optimization with PuLP. Version 2.6.", https://coin-or.github.io/pulp/, 2009.

[36] Gurobi Optimization, LLC, "Gurobi Optimizer Reference Manual", https://www.gurobi.com/documentation/, 2023.

BIOGRAPHIES

José Carlos U. Pena was born in 1984 in Peru. He received the B.S. degree in Electronic Engineering from the National University of Engineering, Lima, Peru, in 2010, and the M.S. and Ph.D. degrees in Electrical Engineering from São Paulo State University, Brazil, in 2012 and 2016, respectively. Since 2022, he is a Researcher with the School of Electrical and Computer Engineering, University of Campinas. His research interests include power electronics, modeling and control of power converters, microgrids, and power quality. Dr. Peña is a member of the SOBRAEP and IEEE.

Jéssica Alice A. Silva was born in 1994 in Brazil. She received the B.S. and M.Sc. degrees in Electrical Engineering from the Federal University of Goiás, Goiânia, Brazil, in 2016 and 2019, respectively, the Ph.D. degree in Electrical Engineering from the University of Campinas, Campinas, Brazil, in 2023. She is currently pursuing a postdoctoral degree at the UNICAMP. Her research interests include modeling, optimizing, analyzing, and controlling distributed energy resources and microgrids and developing methodologies for energy management systems in power systems.

Mateus Pinheiro Dias was born in 1996 in Quixadá, Brazil. He received the B.S.degree in Electrical Engineering from the Federal University of Ceará, Fortaleza, Brazil in 2017. He received the M.Sc. degree in 2020 and is currently pursuing a Ph.D. degree at the University of Campinas, Campinas, Brazil. His research interests include power electronics, More electric Aircraft and dc microgrids. M.Sc. Dias is a student member of the SOBRAEP and IEEE.

Debora Pereira Damasceno was born in 1994 in Fortaleza, Brazil. She received the B.S. and M.Sc. degrees in Electrical Engineering from the Federal University of Ceará, Fortaleza, Brazil, in 2018 and 2021, respectively. She is currently pursuing a Ph.D. degree at the University of Campinas, Campinas, Brazil. Her research interests include power electronics, modeling and control of power converters, and dc microgrids. M.Sc. Damasceno is a student member of the SOBRAEP and IEEE.

Luiza Higino S. Santos was born in 1997 in São Paulo, Brazil. She received a B.S. degree from the Pontifical Catholic University of Campinas in 2019 and an M.Sc. degree at University of Campinas (UNICAMP) in 2022,

both in Electrical Engineering. She is currently pursuing a Ph.D. degree at UNICAMP, Campinas, Brazil. Her research interests include microgrids, strategies for energy management systems, digital twins for distributed energy resources, and protection coordination. M.Sc. Santos is a student member of IEEE.

José Antenor Pomilio was born in Jundiaí, Brazil, in 1960. He received his B.S., M.S., and Ph.D. in Electrical Engineering from the University of Campinas, Campinas, Brazil, in 1983, 1986, and 1991, respectively. From 1988 to 1991, he was the Head of the Power Electronics Group, Brazilian Synchrotron Light Laboratory. He was a visiting professor at the University of Padova in 1993 and 2015 and at the Third University of Rome in 2003 in Italy. He is a Professor at the School of Electrical and Computer Engineering, University of Campinas, where he has been teaching since 1984. His main interests are power electronics and power quality. Dr. Pomilio was the President of the Brazilian Power Electronics Society in 2000–2002 and a member of the Administrative Committee of the IEEE Power Electronics Society in 1997–2002.